Revised atmospheric excitation function series related to Earth's variable rotation under consideration of surface topography

Y. H. Zhou
Shanghai Astronomical Observatory, Chinese Academy of Sciences, Shanghai 200030, China
Atmospheric and Environmental Research, Inc., Lexington, MA 02421, USA

D. A. Salstein
Atmospheric and Environmental Research, Inc., Lexington, MA 02421, USA
NASA/Goddard Space Flight Center//University of Maryland Baltimore Campus, Greenbelt, Maryland 20771, USA

J. L. Chen
Center for Space Research, University of Texas at Austin, Austin, TX 78712, USA

Contact Information:

Dr. Yonghong Zhou
Shanghai Astronomical Observatory,
Chinese Academy of Sciences,
Shanghai 200030, China

Phone: 8621-64386191
Fax: 8621-64384618
Email: yhzhou@shao.ac.cn

Abstract.

The atmospheric angular momentum is closely related to variations in the Earth rotation. The atmospheric excitation function (AEF), known also as the atmospheric effective angular momentum function, is introduced in studying the atmospheric excitation of the Earth's variable rotation. It may be separated into two portions, i.e., the "wind" terms due to the atmospheric motion relative to the mantle and the "pressure" terms due to the variations of atmospheric mass distribution evident through surface pressure changes. The AEF wind terms during the period of 1948-2004 are re-processed from the NCEP/NCAR (National Centers for Environmental Prediction-National Center for Atmospheric Research) reanalysis 6-hourly wind and pressure fields. Some previous calculations were approximate, in that the wind terms were integrated from an isobaric lower boundary of 1000 hPa. To consider the surface topography effect, however, the AEF is computed by integration using the winds from the Earth's surface to 10 hPa, the top atmospheric model level, instead of from 1000 hPa. For these two cases, only a minor difference, equivalent to ~0.004 milliseconds in length-of-day variation, exists with respect to the axial wind term. However, considerable differences, equivalent to 5~6 milliarcseconds in polar motion, are found regarding equatorial wind terms. We further compare the total equatorial AEF (with and without the topographic effect) with the polar motion excitation function (PMEF) during the period of 1980-2003. The equatorial AEF gets generally closer to the PMEF, and improved coherences are found between them when the topography effect is included.

Keywords: Atmospheric excitation function, Atmospheric angular momentum, Earth rotation, Topography, Wind, Pressure.

1. Introduction

The dynamic interactions that occur between atmosphere and solid Earth are related globally by conservation of angular momentum in the Earth system. Due to this condition, the global atmospheric angular momentum variation is closely related to the Earth's variable rotation on time scales between a few days and several years [e.g. Barnes et al., 1983; Eubanks et al., 1988; Chao and Au, 1991; Hide and Dickey, 1991; Zhou et al., 2001]. The atmospheric excitation function (AEF), namely the atmospheric effective angular momentum function in Barnes et al. [1983], is introduced in studying the atmospheric excitation of the Earth's variable rotation. Obtaining accurate calculations of AEF is thus of great interest to the geodetic community, which is concerned with Earth's rotation and its reference frame. The AEF has three components: an axial component, related to the rate of rotation of Earth and measured by length of day (LOD), and two equatorial components, related to the motion of the pole in an Earth-fixed reference frame. Each component has "wind" and "pressure" terms reflecting atmospheric relative angular momentum and the redistribution of global atmospheric mass. The AEF is usually calculated from global atmospheric analysis or reanalysis fields from a four-dimensional data assimilation system that incorporates a heterogeneous set of data and an underlying atmospheric model. These series based on four of the world's major meteorological centers have been archived by the Special Bureau for Atmosphere (SBA) of the Global Geophysical Fluids Center of the International Earth Rotation and Reference Systems Service (IERS) [Salstein et al., 1993; Salstein and Rosen, 1997].

Substantial discrepancies exist among the AEF collected from output of the analyses by several of the world meteorological centers. Hide et al. [1997] stated that the

dominant seasonal error in simulating the axial AEF is an underestimation of AEF during northern hemisphere winter associated with errors in the position of subtropical jets. Eubanks et al. [1988] found that the two equatorial AEF pressure terms from the US National Meteorological Center (NMC) and Japan Meteorological Agency (JMA) have much higher correlation (~0.9) than the wind terms (~0.4). The large disagreements in these equatorial wind terms were attributed in part to a lack of data from sparsely observed regions such as the South Pacific. In the study of atmospheric contributions to the Earth rotation on the seasonal time scale, Aoyama and Naito [2000] demonstrated that the differences in equatorial AEF wind terms between the JMA and the US National Center for Environmental Prediction (NCEP, formerly NMC) / National Center for Atmospheric Research (NCAR) result not only from the discrepancies arising from the different tropospheric regional winds associated with the Asian monsoon, but also from the difference in the vertical integration methods of computing AEF wind terms [Rosen and Salstein, 1985; Naito et al., 1987, 2000].

Here we re-process the AEF during the period of 1948-2004 based on the NCEP/NCAR reanalysis wind and pressure fields [Kalnay et al., 1996]. Some previous calculations for the SBA are approximated, with the winds integrated from an isobaric lower boundary at 1000 hPa. To consider the surface topography effect, however, the AEF is computed here by integration using the winds from the Earth's surface to 10 hPa, the top atmospheric model level, instead of from 1000 hPa. This method has been applied in the computation of JMA AEF by using the surface pressures on land and sea level pressures on oceans [Naito et al., 1987]. In Section 2, we introduce the basic formulas and data processing of the AEF and the Earth rotation excitation function. The comparisons

among the AEF with and without consideration of Earth's topography and the Earth rotation excitations are given in Section 3. We summarize the results in Section 4.

2. Formulation and Data Processing

2.1. Earth Rotation Excitation Function

In the terrestrial coordinate system, the rotation of the Earth can be described by the 3-dimensional instantaneous angular velocity vector of the mantle. Its axial and equatorial components are associated with the variations of the Earth's rotational rate (or the LOD change) and the polar motion, respectively. The Earth's rotation is basically subject to the following excitation equations, under the conservation of the Earth's total angular momentum [Barnes et al., 1983; Eubanks, 1993; Aoyama and Naito, 2000]:

$$\mathbf{m} + (i/\sigma_c)\dot{\mathbf{m}} = \boldsymbol{\psi} \tag{1}$$

$$\dot{m}_3 + \dot{\psi}_3 = 0\,. \tag{2}$$

In equation (1), $\mathbf{m} = m_1 - im_2$ is a dimensionless complex-valued small quantity representing the Earth's polar motion, where subscripts 1 and 2 refer to the x (along the Greenwich Meridian) and y (along the 90°E longitude) coordinates of the terrestrial frame (the negative sign comes from the left-handed coordinate system in the conventional definition of polar motions m_1 and m_2). $\boldsymbol{\psi} = \psi_1 + i\psi_2$ with ψ_1 and ψ_2 being the x and y components, respectively, of the polar motion excitation function (PMEF), $\sigma_c = 2\pi F_c(1 + i/2Q)$ is the complex Chandler frequency, F_c is about 0.843 cycles per year, and Q is the damping factor of the Chandler oscillation. In equation (2), $m_3 = -\Delta\Lambda/\Lambda_0$ is a small dimensionless quantity representing the LOD change, where

Λ_0 and $\Delta\Lambda$ are a standard LOD and its deviation, the subscript 3 refers to the z (along the north pole) coordinate of the terrestrial frame, and ψ_3 is the excitation function for the LOD change.

The observed polar motion time series is from the SPACE2003 [Gross, 2004] EOP time series, produced by the Jet Propulsion Laboratory, which is daily, sampled at midnight, and covers the period 1976-2003. It is produced through a Kalman filter combination of the Earth orientation measurements from advanced space-geodetic techniques including lunar and satellite laser ranging, very long baseline interferometry, and the global positioning system. The PMEF is computed using equation (1) [Wilson, 1985], at a discrete set of time periods, with Q = 179 [Wilson & Vicente, 1990].

2.2 Atmospheric Excitation Function

Similar to the Earth rotation vector, the AEF has equatorial and axial components (χ and χ_3). Each component consists of the pressure term ($\chi^{\mathbf{P}}$, χ_3^P) due to air mass redistribution, and the wind term ($\chi^{\mathbf{W}}$, χ_3^W) due to atmospheric relative angular momentum. They are expressed as follows [Eubanks, 1993]:

$$\begin{aligned}\chi^{\mathbf{P}} &= \chi_1^P + i\chi_2^P \\ &= \frac{-1.098R^4}{(C-A)g}\iint p_s \sin\phi\cos^2\phi e^{i\lambda} d\lambda d\phi\end{aligned} \tag{3}$$

$$\begin{aligned}\chi^{\mathbf{W}} &= \chi_1^W + i\chi_2^W \\ &= \frac{-1.5913R^3}{\Omega(C-A)g}\iiint (u\sin\phi + iv)\cos\phi e^{i\lambda}\mathrm{d}p\mathrm{d}\lambda\mathrm{d}\phi\end{aligned} \tag{4}$$

$$\chi_3^P = \frac{0.753R^4}{C_m g}\iint p_s \cos^3\phi d\lambda d\phi \tag{5}$$

$$\chi_3^W = \frac{0.998R^3}{C_m \Omega g}\iiint u\cos^2\phi \mathrm{d}p\mathrm{d}\lambda\mathrm{d}\phi \ , \tag{6}$$

where R and Ω are the Earth's mean radius and angular velocity, A and C are the Earth's principal moments of inertia, C_m is the mantle's principal moment of inertia, g is gravitational acceleration, λ and ϕ are longitude and latitude at a given grid point, p_s is surface pressure, u and v are the zonal and meridional wind velocities, respectively.

The AEF is computed based on equations (3)-(6), using four-times daily (0000, 0600, 1200 and 1800 GMT) wind and pressure fields for the year of 1948 to 2004, from the NCEP/NCAR reanalysis atmospheric system [Kalnay et al., 1996]. The output is on grid with resolution 2.5° longitude by 2.5° latitude. The wind fields covers 17 pressure levels (1000, 925, 850, 700, 600, 500, 400, 300, 250, 200, 150, 100, 70, 50, 30, 20 and 10 hPa). In calculating wind terms, we compensate the Earth's topography effect by integrating wind from the NCEP model's variable Earth surface pressure level (not 1000 hPa) to the top (10 hPa) of the model [Naito et al., 1987; Aoyama and Naito, 2000]. Therefore, for the integration of winds of bottom layers which are affected by the surface topography, the thickness of air over each gridpoint on the global Earth would be a spatial variable rather than a constant everywhere. In calculating pressure terms, two extreme cases are considered. One is based on the inverted barometer (IB) assumption, which assumes that oceans respond to the atmospheric loading isostatically; the other is a non-inverted barometer (non-IB) assumption, which assumes that oceans behave like a solid surface [Munk and MacDonald, 1960; Salstein et al., 1993]. In order to match the

temporal resolution of the PMEF, the 6-hourly NCEP/NCAR reanalysis AEF is averaged daily by summing five consecutive values using weights of 1/8, 1/4, 1/4, 1/4, 1/8.

3. Results and Comparison

3.1. Comparison between AEF Wind Terms during 1948-2004 with and without Consideration of Surface Topography

The surface topography effect is demonstrated by the comparison between the AEF wind terms with/without the surface topography correction. Figure 1 shows the comparison of equatorial wind terms not accounting for (green curves) and accounting for (red curves) topography (topo) during the period of 1948-2004. The differences of the equatorial wind terms between the non-topo and the topo terms are given in Figure 2. For clarity of display, 30-day moving averages of the 6-hourly data are shown. The standard deviations of the differences are 5.8 and 5.4 milliarcseconds (mas) for χ_1 and χ_2, respectively. Figure 3 displays the comparison of axial wind terms between the non-topo (green curve) and topo (red curve) cases, and the difference between these two terms. The standard deviation of the difference is 0.004 ms. Obviously, only a minor difference between the non-topo and topo cases exists with respect to the axial wind term. However, considerable differences are found regarding the equatorial wind terms. This different characteristic of wind contributions in the axial and equatorial components was also found by Aoyama and Naito [2000] in their study of wind contribution to the Earth's angular momentum budgets on the seasonal time scale. The equatorial wind AEFs are affected by the zonal and meridional wind field in the lower troposphere, while the axial wind AEF is driven mainly by the prevailing zonal wind circulation in the upper troposphere and stratosphere [Peixoto and Oort, 1992]. In this case, the axial component

is influenced relatively little by the wind field inside the surface topography. It should be mentioned that the equatorial pressure term, a strong contributor to polar motion excitation, is unaffected by the lower boundary approximation (see equation 3).

Figure 1 Figure 2 Figure 3

Figures 4 and 5 show mean daily variation patterns (based on 4 synoptic hours: 0, 6, 12, 18) of the equatorial wind terms (χ_1^W and χ_2^W) with/without the surface topography correction (red/green curves and stars) during all twelve months in 2002. Atmospheric tides are known to cause daily variations in wind [Hsu and Hoskins, 1989], which transfer here to variations in polar motion excitation. As can be seen, the daily variation pattern is slightly affected by the surface topography. The noticeable surface topography effect (albeit quite small) at 12:00 UT on the χ_1 wind term is consistent with the finding by Hsu and Hoskins [1989] that the diurnal and semi-diurnal wind signals in the lower troposphere are affected by thermal effects related to local topography and land-sea contrasts. The equatorial wind terms have strong variations with magnitude of 10~20 mas. They are seasonally modulated and appear to have a distinct 'winter mode' (January to February, November to December) and 'summer mode' (April to September). The months of March and October appear to be periods of transition between the summer and winter modes. Also shown in Figure 6 is the mean daily variation pattern of the axial wind term (χ_3^W). It has a very small daily variation with magnitude of ~0.01ms. The surface topography effect on this term is negligible throughout the whole period.

Figure 4 Figure 5 Figure 6

It is interesting to see how the surface topography affects the AEF wind terms. As an example, Figure 7 displays a "snap-shot" of thickness of air (in unit of hPa) of layers

1~7 (1: surface-962.5 hPa; 2: 962.5 – 887.5 hPa; 3: 887.5–775 hPa; 4: 775– 650 hPa; 5: 650–550 hPa; 6: 550–450 hPa; 7: 450–350 hPa) at 0 hour, Jan.1, 2003. The amount of topography in each layer is evident. The thickness of air of Layer 1 (surface layer) reflects clearly the Earth's variable topography. From layer 1 to layer 7, we witness the gradual disappearing of the topography. The influence of the Himalayas Mountains is most significant. It goes as high as into layer 6 and disappears at layer 7.

Figure 7

The surface topography effects on the equatorial wind AEFs are demonstrated in Figures 8 and 9. Figure 8 shows the differences between the non-topo and topo χ_1^W terms integrated in layers 1~7. The mean value has been removed from each series. For clarity of display, 30-day moving averages of the 6-hourly data are shown. As expected, the difference between the non-topo and topo wind terms finally decreases to zero in layer 7. Also shown in Figure 9 are the differences between the non-topo and topo χ_2^W terms. While the strongest annual difference in χ_1^W term appears to be in layer 1 (the surface layer), the strongest annual difference in χ_2^W term appears in layers 2, 3, and 4. The different impact of the surface topography effect for the two equatorial components results from the non-uniform geographical distribution of the global surface topography and the different spatial patterns of weighting functions given in equation 4.

Figure 8 **Figure 9**

3.2. Comparison among the AEFs during 1980-2003 with and without Consideration of Surface Topography and the PMEF

The effect of the Earth's topography on the AEF is revealed by the comparison among the equatorial AEFs during 1980-2003 with and without consideration of surface

topography and the PMEF. The comparison for the axial component is omitted as it is affected by topography only in a negligible way. The period of comparison is selected starting from 1980 in consideration that the polar motion observations are greatly enhanced due to applications of modern space geodetic techniques [Gross, 2004]. The meteorological analyses have been enhanced as well by the introduction of space-based observations around that date.

3.2.1. Power and Coherence Spectrum Analysis

The surface topography effect on the equatorial wind AEFs is revealed by the power and coherence spectrum analyses in the frequency domain. Figure 10 shows the power spectra of the equatorial AEF wind terms, W(non-topo) and W(topo), computed by the multi-taper method. A linear term has been removed from each series prior to the spectral analysis in the frequency domain. The multi-taper technique was first introduced by Thomson [1982], i.e., several windows are added to the time series prior to the Fourier transformation. Although it degrades the spectral resolution, it greatly reduces the spectral leakage and hence provides more reliable spectral estimates [Chao et al., 1995]. It can be seen from Figure 10 that the W(topo) term has generally more power than the W(non-topo) term except at the annual period (1 cycle/year) for the x-component. Figure 11 shows the power spectra of differences between the W(topo) and W(non-topo) terms. Obviously, there are considerable differences over a broad frequency band, in which the largest differences exist in the annual frequency. Although Figure 10 shows that the annual x-component appears to have a larger difference in amplitude between the topo and non-topo terms than does the y-component, owing to the greater annual phase difference for the y-component than for the x-component, the difference plots in Figure

11 shows that the y-component has the larger annual difference between the topo and non-topo terms than does the x-component.

Figure 10 Figure 11

Further comparisons between the AEF (with and without consideration of surface topography) and the PMEF are displayed in Figure 12. The total of AEF wind term and IB pressure term are compared with polar motion excitations. Apparently, considerable discrepancies remain between the AEF and PMEF, which indicate non-atmospheric sources to the polar motion excitation exist, like global oceans and continental water storage change [Chao and Zhou, 1999; Johnson et al., 1999; Ponte and Stammer, 1999; Gross et al., 2003; Chen et al., 2004; Chen and Wilson, 2005; Zhou et al., 2005]. Moreover, it's interesting to note that adding topography effect brings the AEF generally closer to the PMEF, though only slightly at most frequencies.

Figure 12

To reveal further the topography effect on the annual component of polar motion excitation, shown in Figure 12, we extract the annual component by fitting a linear combination of a trend, annual, semiannual and terannual terms to the AEFs and PMEF in a least squares sense. Table 1 lists the results of this fit for the amplitude A and phase α of the prograde (subscript p) and retrograde (subscript r) components of the excitation of annual polar motion defined by [Munk and MacDonald, 1960]

$$\boldsymbol{\chi(t)} = A_p e^{i\alpha_p} e^{i\sigma(t-t_0)} + A_r e^{i\alpha_r} e^{-i\sigma(t-t_0)} \quad , \qquad \textbf{(7)}$$

where σ is the annual frequency and the reference date t_0 is 1 January 1980, 0000UT. As is consistent with previous studies [e.g., Gross et al., 2003], for both the prograde and retrograde components, the surface pressure variation is seen to be the dominant excitation mechanism, being more than 5 times as large as the effect of wind based on the NCEP/NCAR reanalysis. The European Centre for Medium-Range Weather Forecasts (ECMWF) and JMA wind AEF shows larger contribution to the annual wobble [e.g. Masaki and Aoyama, 2005]. The inclusion of surface topography leads to amplitude reductions of ~30% and phase changes of 41^o and 106^o for the prograde and retrograde wind terms, respectively. The total of AEF pressure and wind terms with consideration of surface topography effect appears to be closer to the annual PMEF than that without consideration of surface topography. Figure 13 shows the phasor diagram of the prograde (top) and retrograde (bottom) annual components of the AEF and PMEF. Apparently, adding topography effect brings the AEF closer to the PMEF on the annual time scale, which is particularly different for the retrograde component.

Table 1

Figure 13

Figure 14 exhibits the multi-taper squared coherences between the AEF (with and without consideration of surface topography) and the PMEF in the frequency domain. A trend and a seasonal signal are removed from each series prior to the coherence analysis. The horizontal dashed line represents the 95% significance level. The vertical dashed line indicates the Chandler frequency of 0.843 cycles per year. When the topography effect is considered, generally improved coherences between the total equatorial AEF and the PMEF are found over a broad frequency band with respect to the x-component, though marginal improvements are seen with respect to the y-component. The improved

coherences around the Chandler frequency are also evident, which confirms the previous finding of Aoyama [2005]. Further analysis on the time domain is given in the following section.

Figure 14

3.2.2. Correlation and Variance Analysis

The surface topography effect on the equatorial wind AEFs is revealed by the correlation and variance analyses in the time domain. We first remove from the AEF and PMEF a linear combination of a trend, annual, semiannual and terannual terms that was fitted by the least squares method. Then, the residual series is passed through a Butterworth high-pass filter of order 2, in both forward and reverse directions to eliminate any phase distortion [Wiley, 1979]. The cutoff frequency is 1 cycle per year. Thus the resulting series is considered as the intraseasonal variation used in the following cross correlation and variance analyses.

Table 2 assembles the cross correlation coefficients between the intraseasonal PMEF and AEF, and variance reductions (in percentage) when the atmospheric effects are removed from the PMEF. X and Y give results for the x and y components, and X+iY for the complex-values x+iy component. The surface pressure variation and winds are both important excitation mechanisms to the intraseasonal polar motion. The surface pressure variation can explain 35.4% of the polar motion excitation and the correlation between them reaches 0.6. After the surface topography effect is included, the correlation between the PMEF and the sum of AEF pressure and wind goes slightly higher (from 0.60 to 0.63, 0.70 to 0.71, and 0.68 to 0.69 for x, y, and x+iy components, respectively) which confirms the frequency-domain coherence analyses in section 3.2.1. Moreover, the

total atmospheric effect can explain 3%, 2.4%, and 2.5% more observed x, y, and x+iy components, respectively, of the intraseasonal polar motion excitation. Gross et al. [2003] illustrated that the global oceans, as the second important source other than the atmosphere, can explain about 20% of the intraseasonal polar motion excitation. Then, the contribution from the surface topography on the polar motion reaches equivalently over 1/10 of that of global oceans, which could be useful to closure of the Earth's angular momentum budget in the future.

Table 2

4. Summary

In this study, the AEF wind terms during the period of 1948-2004 are re-processed using the NCEP/NCAR reanalysis 6-hourly wind and pressure fields (products available at IERS SBA website, http://www.aer.com/scienceResearch/diag/sb.html). Some previous calculations with the NCEP/NCAR reanalyses are approximate, in that the wind terms are integrated from an isobaric lower boundary at 1000 hPa. To consider the Earth's topography effect, however, the AEF is computed by integration using the winds from the NCEP model's representation of the Earth's surface pressure level to the top (10 hPa) analysis level. With respect to these two cases, only a minor difference, equivalent to ~0.004 milliseconds in LOD, exists in the axial wind term. However, considerable differences, equivalent to 5~6 milliarcseconds in polar motion, are found in the equatorial wind terms. We show how Earth's topography in various layers contributes to this wind effect. We further compare the equatorial AEF, with and without the topographic effect, to the polar motion excitation during the period of 1980-2003. The equatorial AEF gets generally closer to the polar motion excitation, and improved coherences are found between them when the topography effect is included.

Acknowledgments. We are grateful to three anonymous reviewers for their insightful comments, which led to improvements in the presentation. We thank Drs. B.F. Chao and R. Ponte for their helpful discussions. Special thanks went to the Descartes-Nutation Committee, with chair, V. Dehant, Royal Observatory of Belgium, for having supported Y.H. Zhou's stay at AER for this study. Y.H. Zhou was supported in part by the National Natural Science Foundation of China (10273018, 10133010) and the Key Project of Chinese Academy of Sciences (KJCX2-SW-T1). D.A. Salstein was supported in part by the U.S. National Science Foundation (under grant ATM-0429975) and both he and J.L. Chen were supported by the NASA Solid Earth and Natural Hazards Program (under grants NNG04G060G, NNG04GP70G). D.A. Salstein was a visiting scientist at NASA through the University of Maryland Baltimore County GEST program during part of the study.

References:

Aoyama Y., and I. Naito (2000), Wind contribution to the Earth's angular momentum budgets in seasonal variation, *J. Geophys. Res.*, 105, 12417-12431.

Aoyama Y. (2005), Quasi-14 month wind fluctuation and excitation of the Chandler wobble, in *Proceedings of the Chandler Wobble Workshop 2004*, European Center for Geodynamics and Seismology, Luxembourg.

Barnes, R., R. Hide, A. White, and C. R. Wilson (1983), Atmospheric angular momentum functions, length-of-day changes and polar motion, *Proc. R. Soc. Lond.*, 387, 31-73.

Chao, B. F., and A. Y. Au (1991), Atmospheric excitation of the Earth's annual wobble: 1980-1988, *J. Geophy. Res.*, 96, 6577-6582.

Chao, B. F., J. B. Merriam, and Y. Tamura (1995), Geophysical analysis of zonal tidal signals in length of day, *Geophys. J. Int.*, 122, 765-775.

Chao, B. F., and Y. H. Zhou (1999), Meteorological excitation of interannual polar motion by the North Atlantic Oscillation, *J. Geodyn.*, 27,61-73.

Chen, J. L., C. R. Wilson, X. G. Hu, Y. H. Zhou and B. D. Tapley (2004), Oceanic effects on polar motion determined from an ocean model and satellite altimetry: 1993-2001, *J. Geophys. Res.*, 109, B02411, doi:10.1029/2003JB002664.

Chen, J. L., and C. R. Wilson (2005), Hydrological excitations of polar motion, 1993-2002, *G. J. Internat.*, 160, 833-839.

Eubanks, T. M., J. A. Steppe, J. O. Dickey, R. D. Rosen, and D. A. Salstein (1988), Causes of rapid motions of the Earth's pole, *Nature*, 334, 115-119.

Eubanks, T. M. (1993), Variations in the orientation of the earth, in *Contributions of Space Geodesy to Geodynamic: Earth Dynamics*, Geodyn. Ser., edited by D. Smith and D. Turcotte, pp. 1-54, AGU, Washington, D.C.

Gross, R. S., I. Fukumori, and D. Menemenlis (2003), Atmospheric and oceanic excitation of the Earth's wobbles during 1980-2000, *J. Geophys. Res.*, 108, B2370, doi:10.1029/2002JB002143.

Gross, R. S. (2004), Combinations of Earth orientation measurements: SPACE2003, COMB2003, and POLE2003, *JPL Publ.*, 04-12.

Hide, R. and J. O. Dickey (1991), Earth's variable rotation, *Science*, 253, 629-637.

Hide, R., J. O. Dickey, S. L. Marcus, R. D. Rosen, and D. A. Salstein (1997), Atmospheric angular momentum fluctuations during 1979-1988 simulated by global circulation models, *J. Geophys. Res.*, 102, 16423-16438.

Hsu, H. H., and B. J. Hoskins (1989), Tidal fluctuations as seen in ECMWF data, *Q.J.R.Meterol. Soc.*, 115, 247-264.

Johnson, T. J., C. R. Wilson, and B. F. Chao (1999), Oceanic angular momentum variability estimated from the parallel ocean climate model, 1988-1998, *J. Geophy. Res.*, 104, 25183-25195.

Kalnay, E., et al. (1996), "The NCEP/NCAR 40-year reanalysis project," *Bull. Am. Meteor. Soc.*, 77, 437-471.

Masaki, Y., and Y. Aoyama (2005), Seasonal and non-seasonal AAM functions from different reanalysis data sets, in *Proceedings of the Chandler Wobble Workshop 2004*, European Center for Geodynamics and Seismology, Luxembourg.

Munk, W. H. and G. J. F. MacDonald (1960), *The rotation of the Earth: a geophysical discussion*, Cambridge University Press, New York.

Naito, I., N. Kikuchi, and K. Yokoyama (1987), Results of estimating the atmospheric effective angular momentum functions based on the JMA global analysis data, *Publ. Int. Latitude Obs. Mizusawa*, 20, 1-11.

Naito, I., Y. H. Zhou, M. Sugi, R. Kawamura, and N. Sato (2000), Three-dimensional atmospheric angular momentum simulated by the japan meteorological agency model for the period of 1955-1994, *J. Meteor. Soc. Japan*, 78, 111-122.

Peixoto, J. P. and A. H. Oort (1992), *Physics of climate*, American Institute of Physics, New York.

Ponte, R. M., and D. Stammer (1999), Role of ocean currents and bottom pressure variability on seasonal polar motion, *J. Geophys. Res.*, 104, 23393-23410.

Rosen, R. D., and D. A. Salstein (1985), Contribution of stratospheric winds to annual and semiannual fluctuations in atmospheric angular momentum and the length of day, *J. Geophys. Res.*, 90, 8033-8041.

Salstein, D. A., D. M. Kann, A. J. Miller, and R. D. Rosen (1993), The sub-bureau for atmospheric angular momentum of the interannual earth rotation service: a meteorological data center with geodetic applications, *Bull. Am. Meteor. Soc.*, 74, 67-80.

Salstein, D. A., and R. D. Rosen (1997), Global momentum and energy signals from reanalysis systems. Preprints, in *7th Conf. on Climate Variations*, American Meteorological Society, Boston, MA, 344-348.

Thomson, D. J. (1982), Spectrum estimation and harmonic analysis, *IEEE. Proc.*, 70, 1055-1096.

Wiley, J. (1979), *Programs for digital signal processing*, IEEE Press, New York.

Wilson, C. R. (1985), Discrete polar motion equations, *Geophys. J. R. astr. Soc.*, 80, 551-554.

Wilson, C. R. and R. O. Vicente (1990), Maximum likelihood estimates of polar motion parameters. In *Variations in Earth Rotation*, pp. 151-155, eds McCarthy, D.D. & Carter, W.E., Am. Geophys. Un. Geophys Monogr. Series, Washington, DC.

Zhou, Y. H., D. W. Zheng, N. H. Yu, and X. H. Liao (2001), Movement of Earth rotation and activities of atmosphere and ocean, *Chin. Sci. Bull.*, 46, 881-888.

Zhou, Y. H., J. L. Chen, X. H. Liao, and C. R. Wilson (2005), Oceanic excitations on polar motion: a cross comparison among models, *Geophys. J. Int.*, 162, 390-398.

Figure captions:

Figure 1. The equatorial wind terms (χ_1 and χ_2) of the atmospheric excitation function (AEF) with/without the surface topography correction (red/green curves) during the period of 1948-2004. For clarity of display, 30-day moving averages of the 6-hourly data are shown. W(non-topo): AEF wind term without consideration of surface topography; W(topo): AEF wind term with consideration of surface topography.

Figure 2. Differences between the non-topo and topo equatorial wind terms (χ_1 and χ_2) shown in Figure 1.

Figure 3. The non-topo (green curve) and topo (red curve) axial wind term (χ_3) during the period of 1948-2004 (top) and the difference between these two terms (bottom).

Figure 4. Mean daily variation pattern of the equatorial wind term (χ_1^W) with/without the surface topography correction (red/green curves and stars) during all twelve months in 2002.

Figure 5. As in Fig.4 but for the χ_2^W term.

Figure 6. As in Fig.4 but for the χ_3^W term.

Figure 7. The surface topography shown by the thickness of air (in unit of hPa) in layers 1~7 (1: surface-962.5 hPa; 2: 962.5 – 887.5 hPa; 3: 887.5–775 hPa; 4: 775– 650 hPa; 5: 650–550 hPa; 6: 550–450 hPa; 7: 450–350 hPa).

Figure 8. Surface topography effects on the equatorial wind AEFs shown by differences between the non-topo and topo χ_1^W terms from layers 1 to 7. The mean value has been removed from each series. For purposes of clarity of display, 30-day moving averages of the 6-hourly data are shown.

Figure 9. As in Fig.8 but for the χ_2^W term.

Figure 10. Multi-taper power spectral density estimates in decibels (unit: mas^2/cpy) of W(non-topo) and W(topo) for x-components (top) and y-components (bottom). A linear term is removed from each series prior to the power spectrum computation.

Figure 11. Surface topography effects on the equatorial wind AEFs in the frequency domain, shown by multi-taper power spectral density estimates in decibels (unit: mas^2/cpy) of the difference between W(topo) and W(non-topo) for x-components (top) and y-components (bottom).

Figure 12. Multi-taper power spectral density estimates in decibels (unit: mas^2/cpy) of OBS (green curves), P+W(non-topo) (blue curves) and P+W(topo) (red curves) for x-components (top) and y-components (bottom). A linear term is removed from each series before the computation of the power spectrum. OBS: the polar motion excitation function (PMEF) inferred from SPACE2003 polar motion; P: the AEF pressure term under the inverted barometer (IB) assumption.

Figure 13. Phasor diagrams of the prograde and retrograde components of annual AEF and PMEF.

Figure 14. Multi-taper squared coherences for x-components (top) and y-components (bottom) between the PMEF spanning 1980-2003 and the excitation functions due to P+W(non-topo) (blue curves) and P+W(topo) (red curves). A trend and a seasonal signal have been removed from each series prior to the coherence analysis. The horizontal dashed line represents the 95% significance level. The vertical dashed line indicates the Chandler frequency of 0.843 cycles per year.

Table 1. Amplitude and phase of the prograde and retrograde components of the annual atmospheric excitation function (AEF) and polar motion excitation function (PMEF). The reference date for phase is 1 January 1980, 0000UT.

	Annual Prograde		Annual Retrograde	
Excitation function	Ampli., mas	Phase, deg	Ampli., mas	Phase, deg
OBS	14.93	-59.1	7.81	-125.1
P	14.85	-101.3	15.12	-107.4
W(non-topo)	2.64	-39.9	1.89	-2.8
W(topo)	1.75	1.1	1.32	102.9
P+W(non-topo)	16.27	-93.1	14.75	-100.3
P+W(topo)	14.57	-94.6	14.00	-110.1

OBS: the PMEF inferred from SPACE2003 polar motion; P: the AEF pressure term under the inverted barometer assumption; W(non-topo): AEF wind term without consideration of surface topography; W(topo): AEF wind term with consideration of surface topography.

Table 2. Cross correlation coefficients between the intraseasonal PMEF and AEF, and variance reductions (in percentage) when the atmospheric effects are removed from the PMEF.

	X		Y		X + i Y	
AEF	Corr. Coef.	Reduced Var. (%)	Corr. Coef.	Reduced Var. (%)	Corr. Coef.	Reduced Var. (%)
P	0.44	18.8	0.65	41.9	0.60	35.4
W(non-topo)	0.47	21.4	0.51	19.4	0.48	19.9
W(topo)	0.50	24.8	0.50	21.5	0.49	22.4
P+W(non-topo)	0.60	35.5	0.70	48.5	0.68	44.9
P+W(topo)	0.63	38.5	0.71	50.9	0.69	47.4

X: x component; Y: y component;

Corr. Coef.: Correlation coefficient; Reduced Var.: Reduced variance;

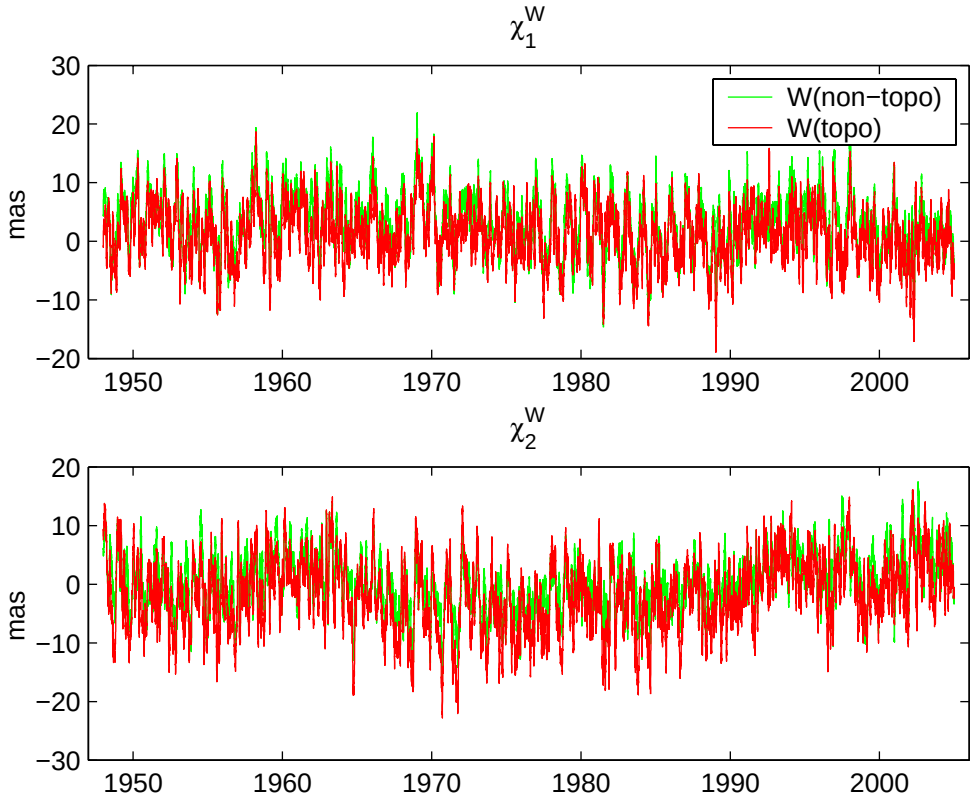
χ_1^W
W(non−topo)
W(topo)
mas
30
20
10
0
−10
−20
1950
1960
1970
1980
1990
2000
χ_2^W
mas
20
10
0
−10
−20
−30
1950
1960
1970
1980
1990
2000

Figure 1

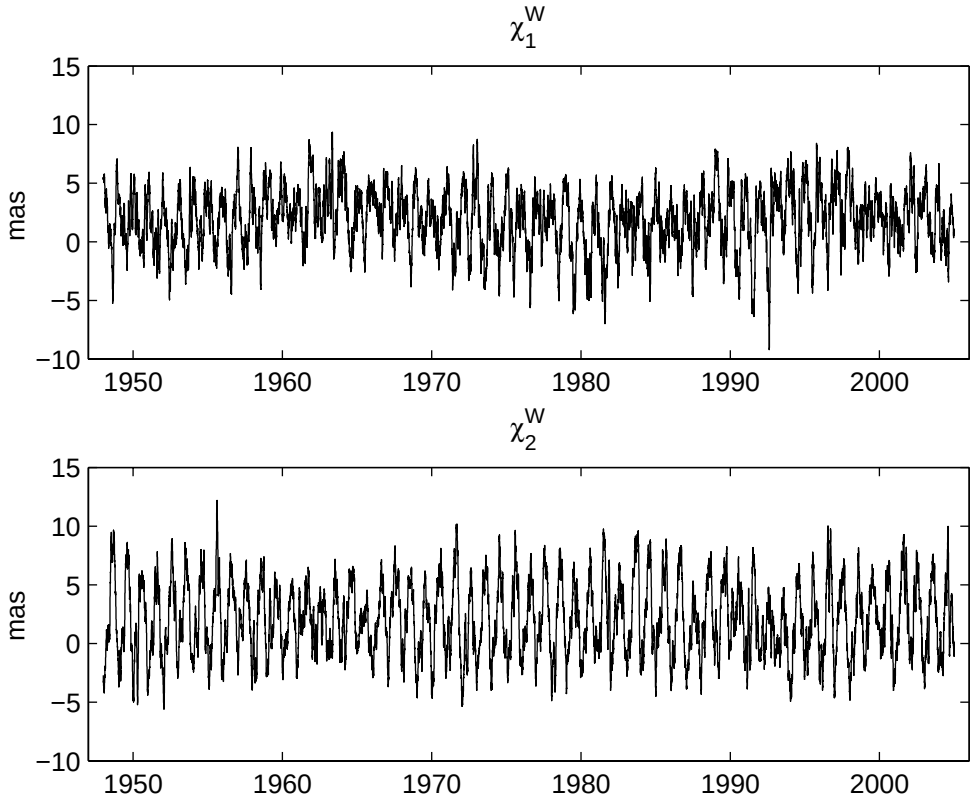
χ_1^W
15
10
5
0
−5
−10
mas
1950
1960
1970
1980
1990
2000
χ_2^W
15
10
5
0
−5
−10
mas
1950
1960
1970
1980
1990
2000

Figure 2

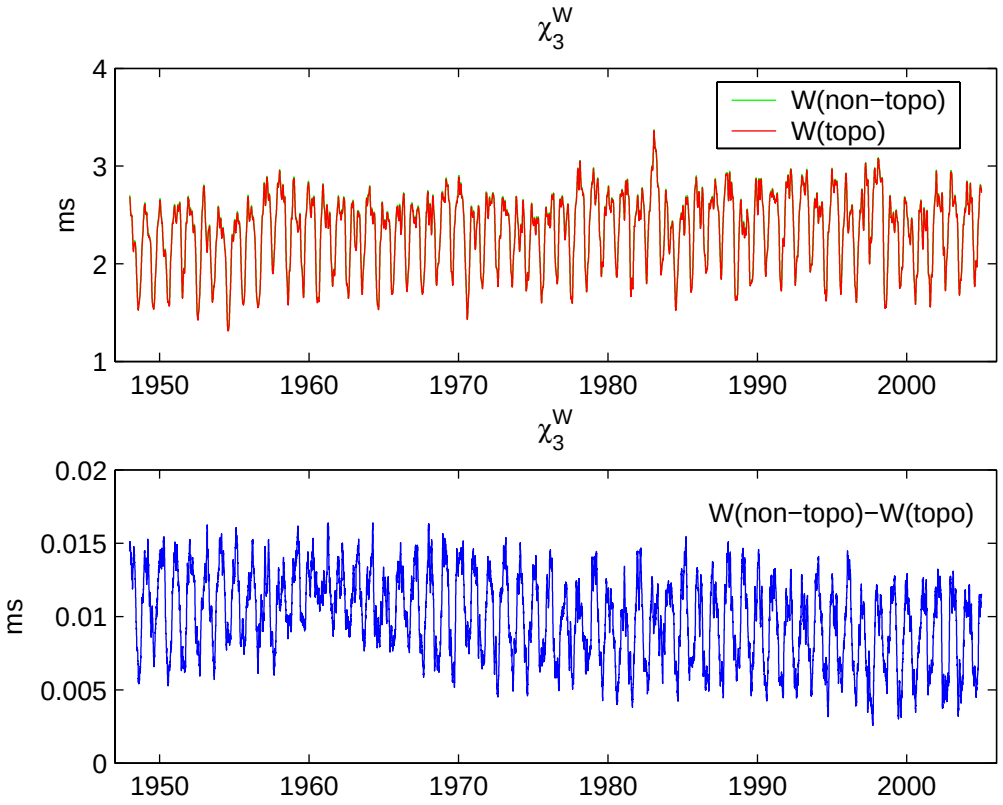
χ_3^W
W(non−topo)
W(topo)
ms
4
3
2
1
1950
1960
1970
1980
1990
2000
χ_3^W
W(non−topo)−W(topo)
ms
0.02
0.015
0.01
0.005
0
1950
1960
1970
1980
1990
2000

Figure 3

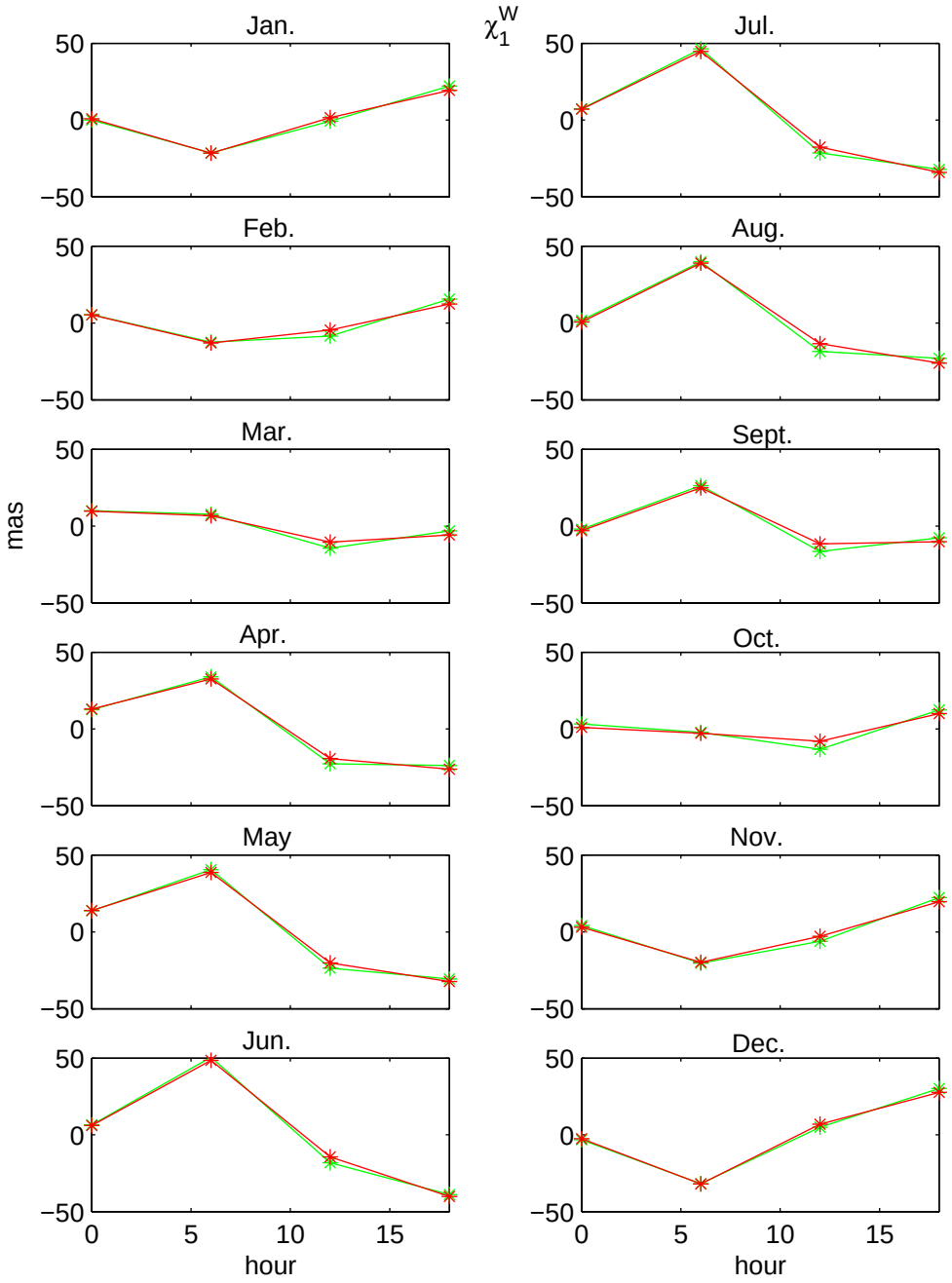
χ_1^W
Jan.
Feb.
Mar.
Apr.
May
Jun.
Jul.
Aug.
Sept.
Oct.
Nov.
Dec.
mas
hour
hour
50
0
−50
0
5
10
15

Figure 4

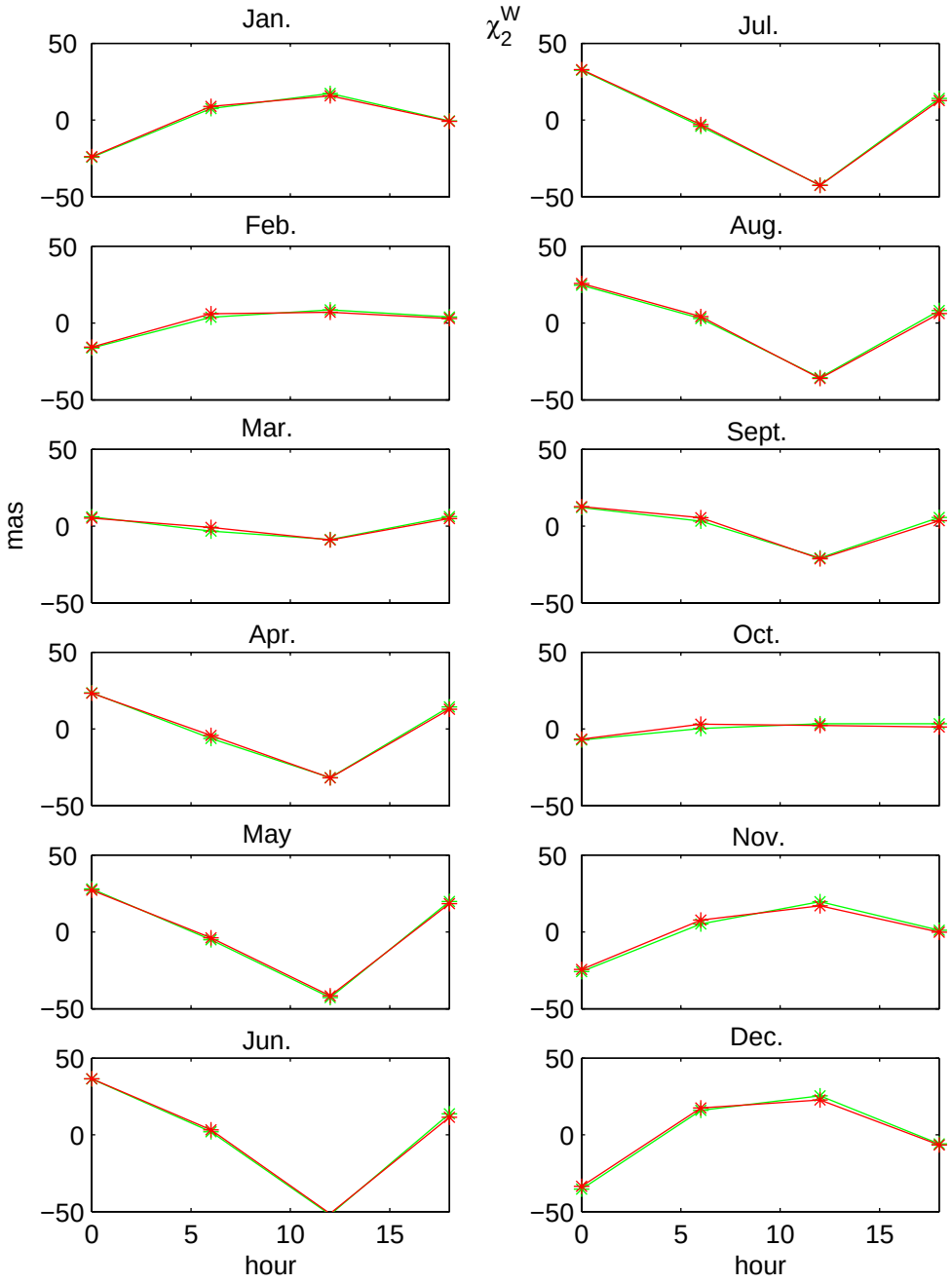
Jan.
Feb.
Mar.
Apr.
May
Jun.
Jul.
Aug.
Sept.
Oct.
Nov.
Dec.
mas
hour
hour
50
0
−50
0
5
10
15
χ_2^W

Figure 5

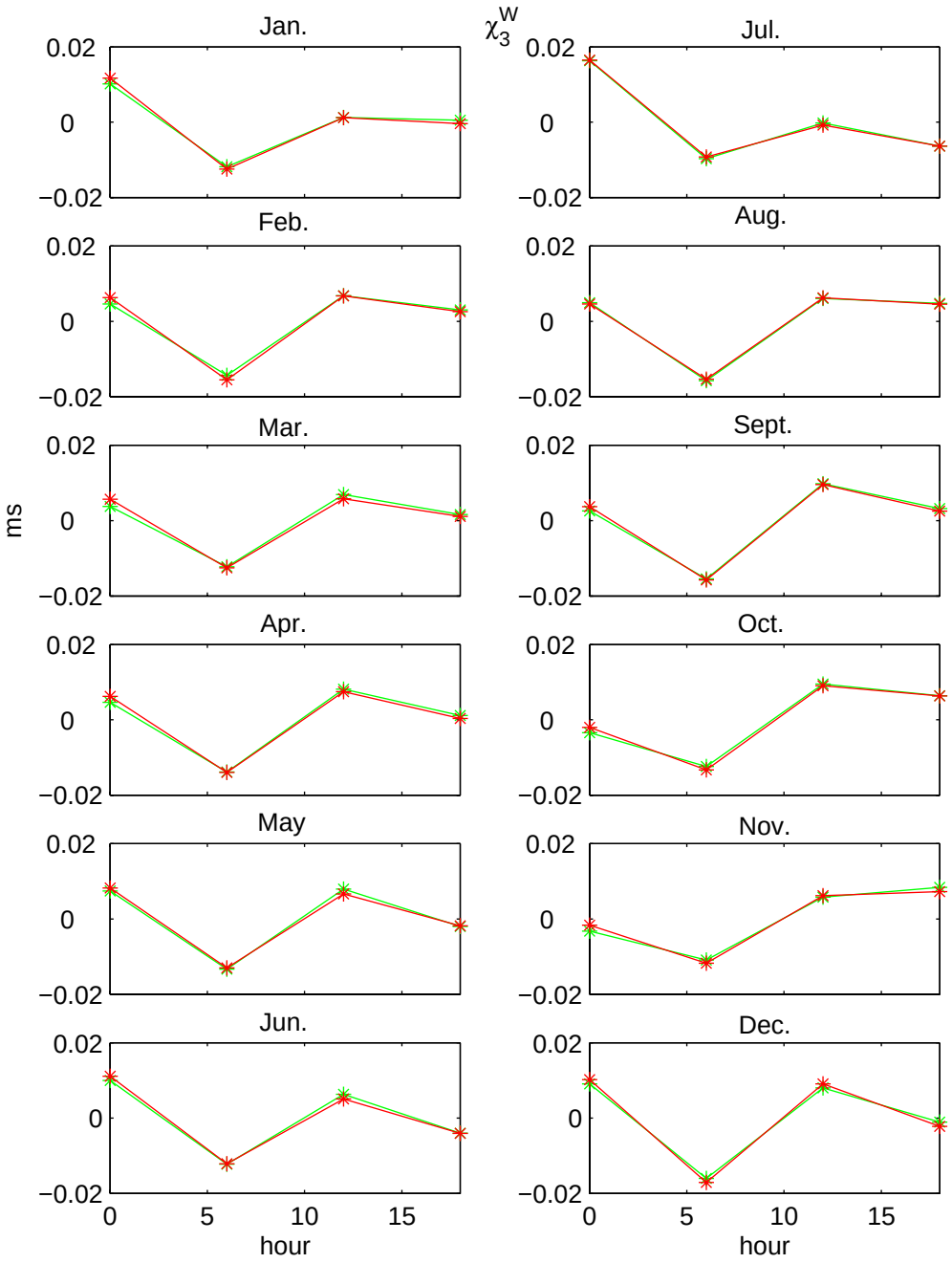
χ_3^W
ms
Jan.
Feb.
Mar.
Apr.
May
Jun.
Jul.
Aug.
Sept.
Oct.
Nov.
Dec.
0.02
0
−0.02
0
5
10
15
hour

Figure 6

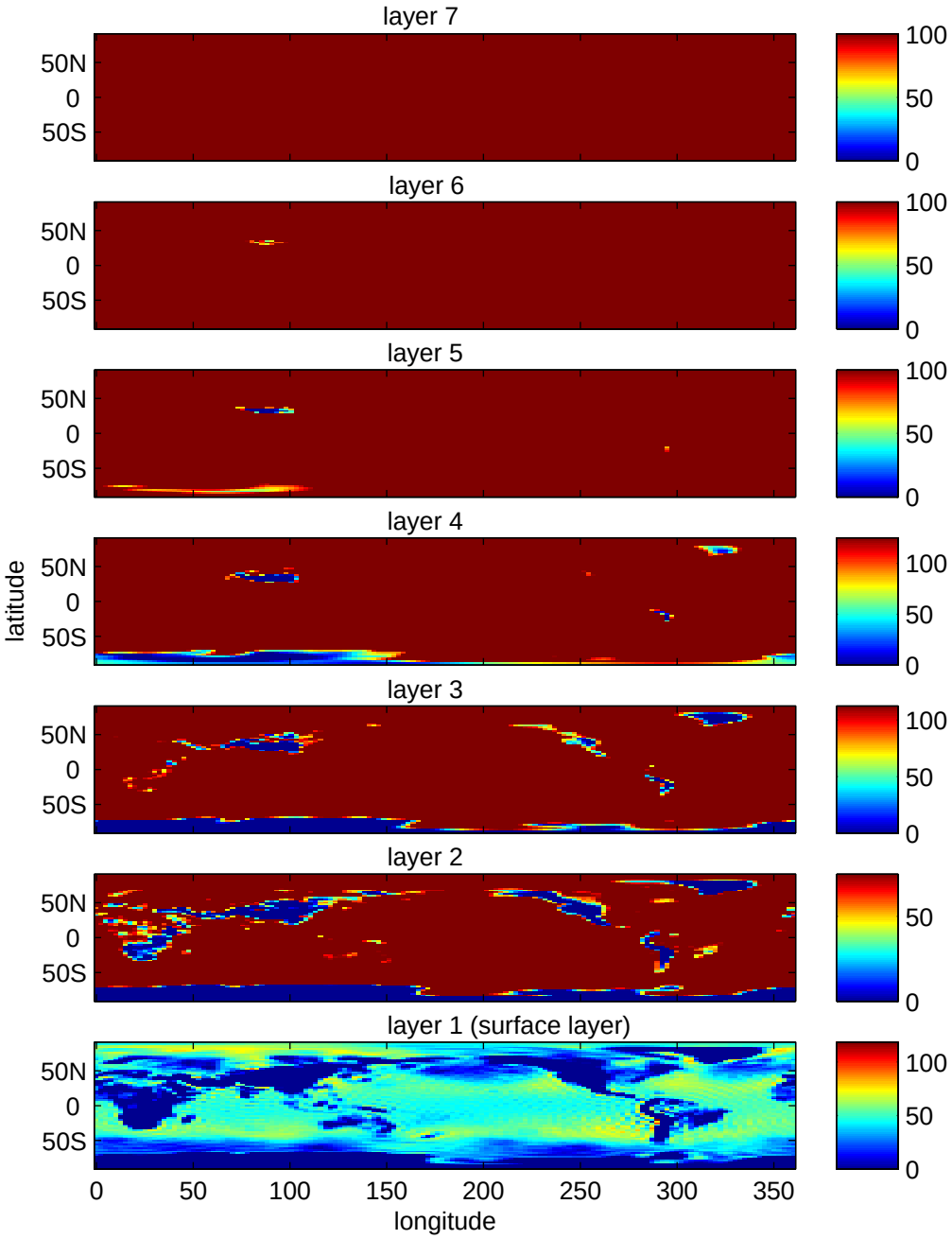
layer 7
layer 6
layer 5
layer 4
layer 3
layer 2
layer 1 (surface layer)
50N
0
50S
100
50
0
latitude
0
50
100
150
200
250
300
350
longitude

Figure 7

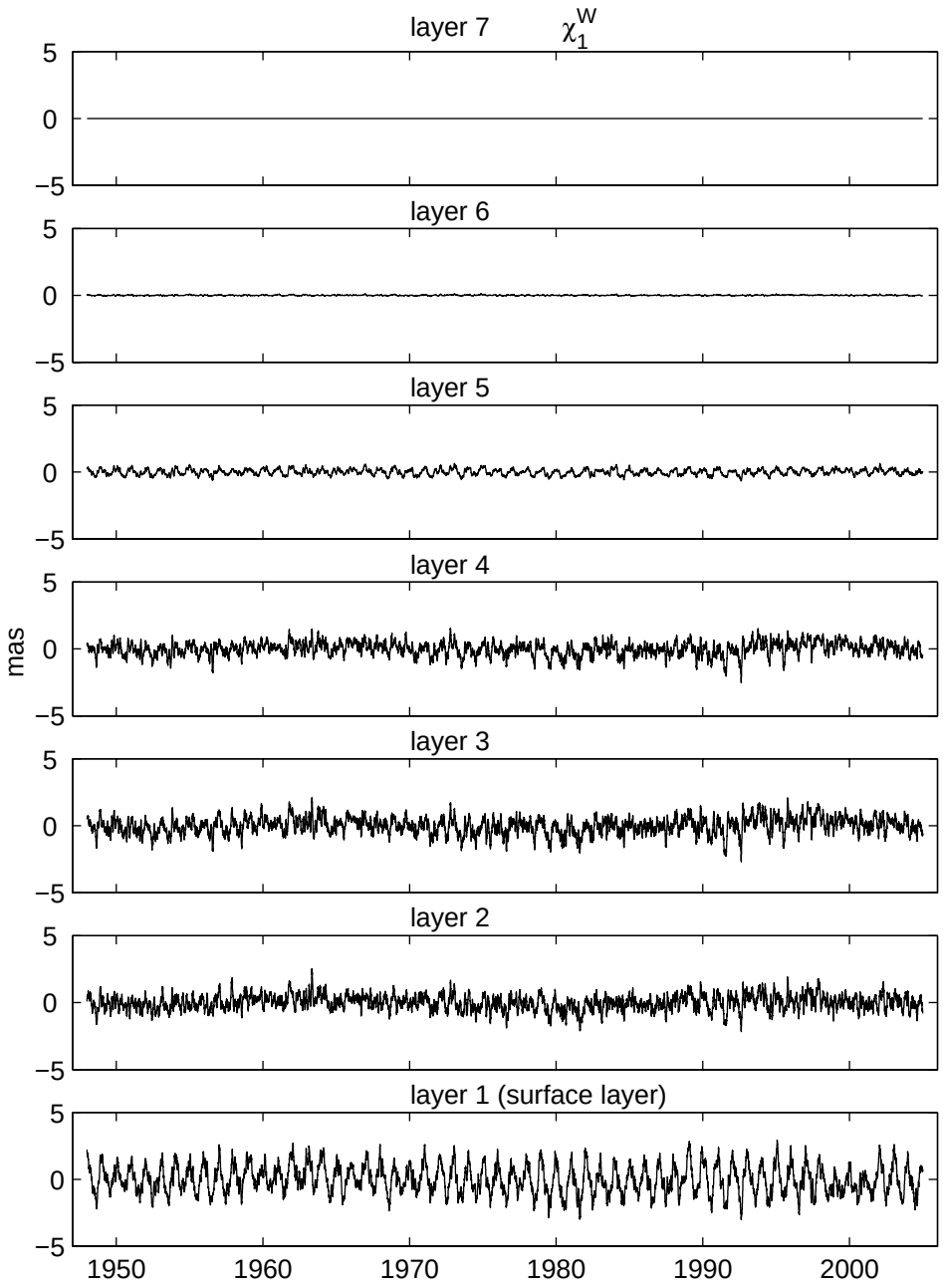
layer 7
χ_1^w
layer 6
layer 5
layer 4
layer 3
layer 2
layer 1 (surface layer)
mas
5
0
−5
1950
1960
1970
1980
1990
2000

Figure 8

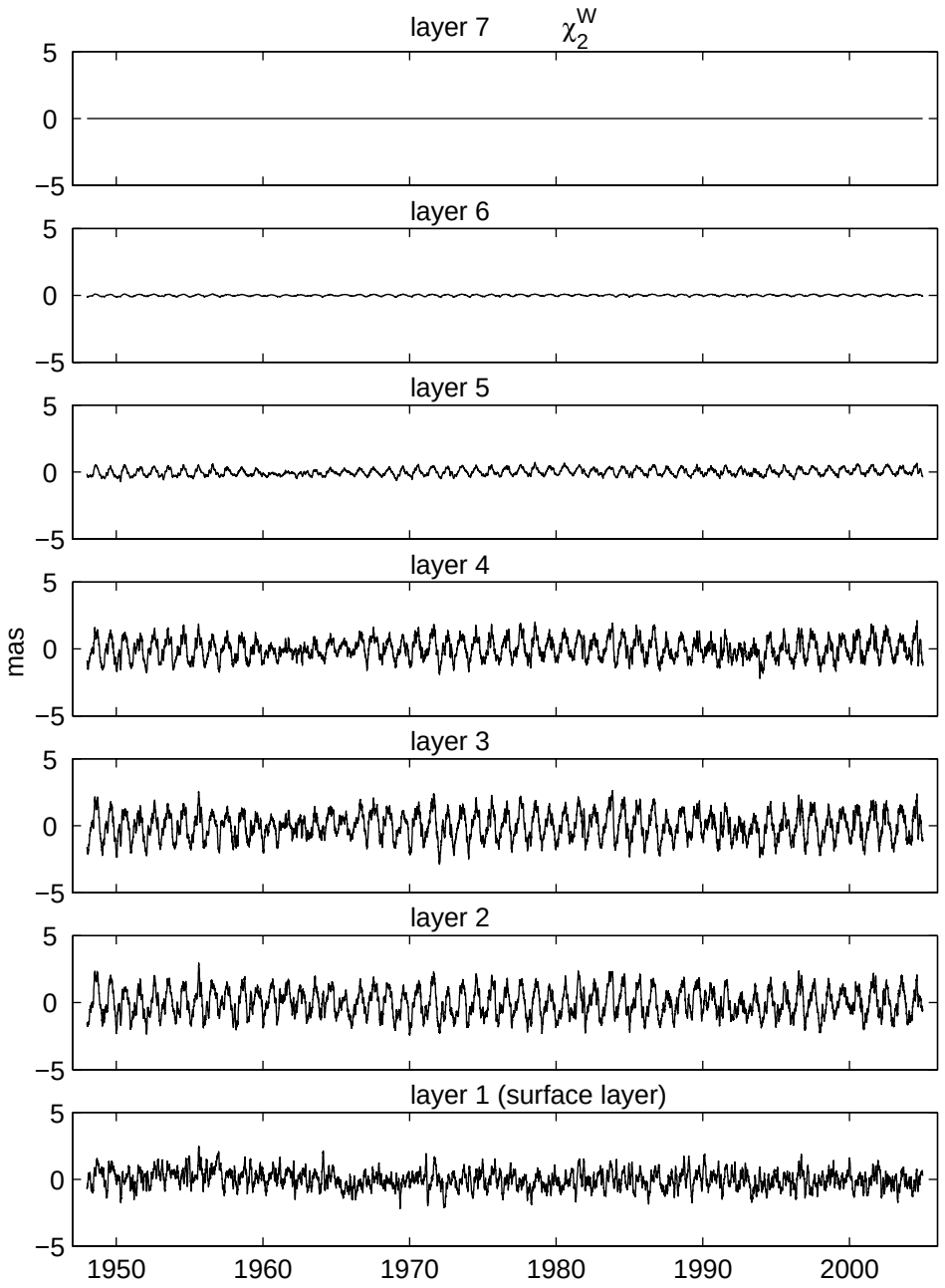
layer 7
χ_2^W
layer 6
layer 5
layer 4
layer 3
layer 2
layer 1 (surface layer)
mas
5
0
−5
1950
1960
1970
1980
1990
2000

Figure 9

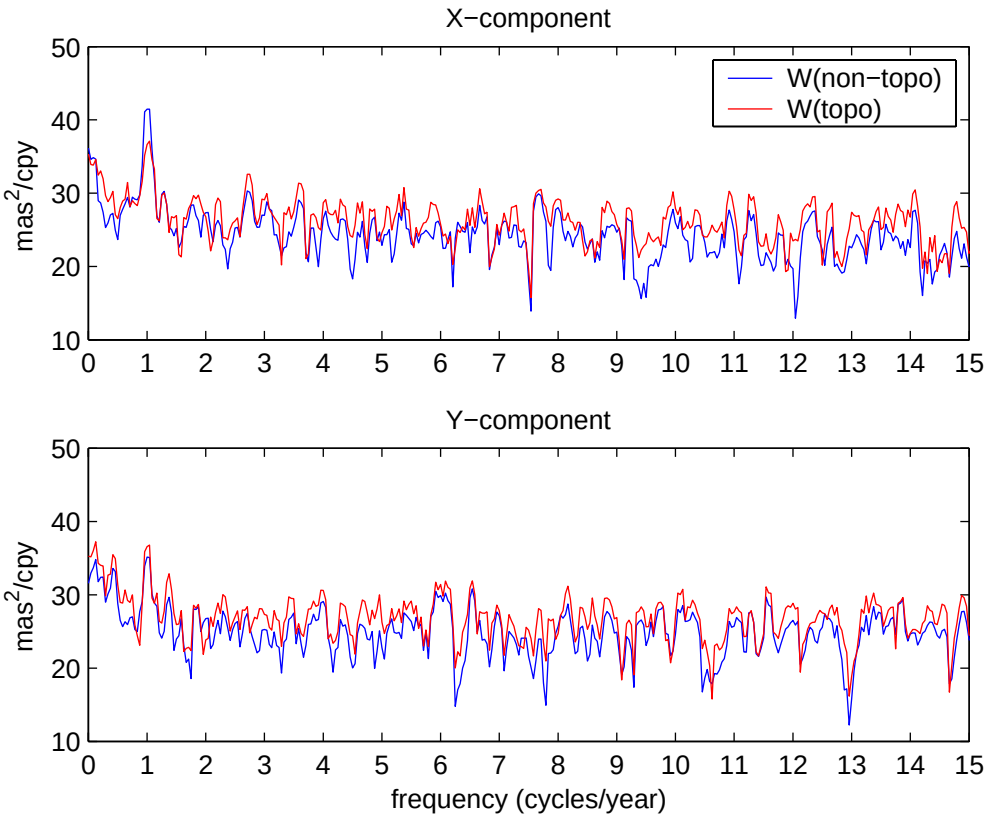
X−component
W(non−topo)
W(topo)
mas²/cpy
50
40
30
20
10
0 1 2 3 4 5 6 7 8 9 10 11 12 13 14 15
Y−component
mas²/cpy
50
40
30
20
10
0 1 2 3 4 5 6 7 8 9 10 11 12 13 14 15
frequency (cycles/year)

Figure 10

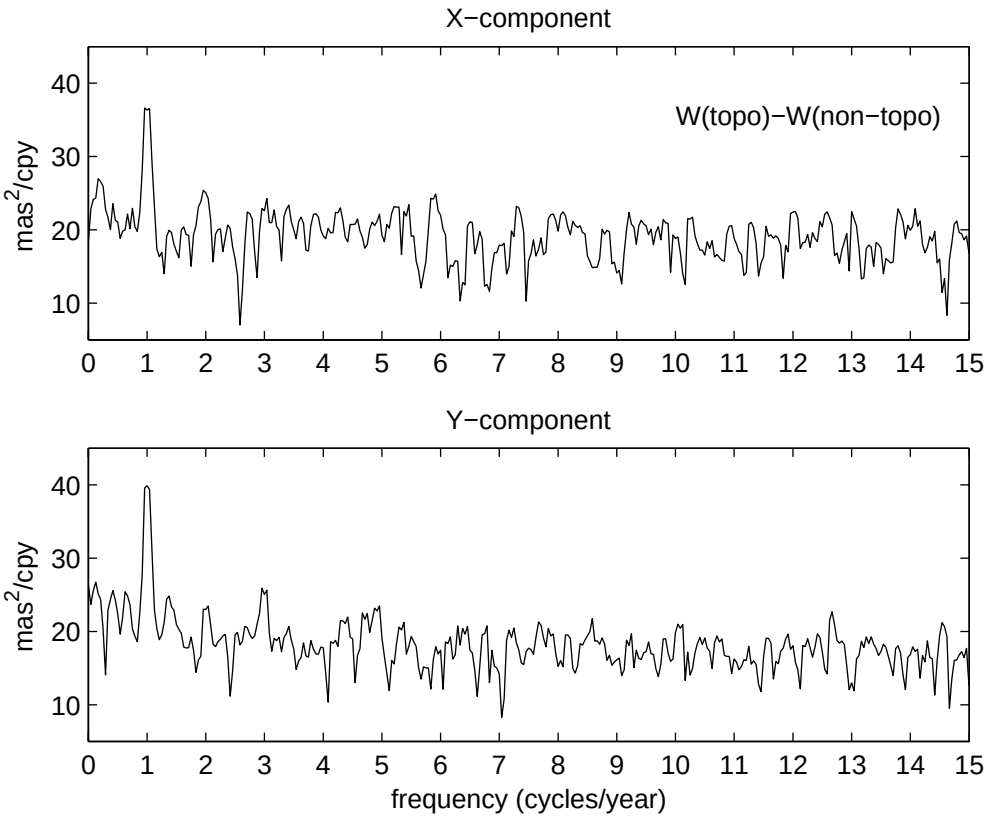
X−component
W(topo)−W(non−topo)
mas²/cpy
40
30
20
10
0 1 2 3 4 5 6 7 8 9 10 11 12 13 14 15
Y−component
mas²/cpy
40
30
20
10
0 1 2 3 4 5 6 7 8 9 10 11 12 13 14 15
frequency (cycles/year)

Figure 11

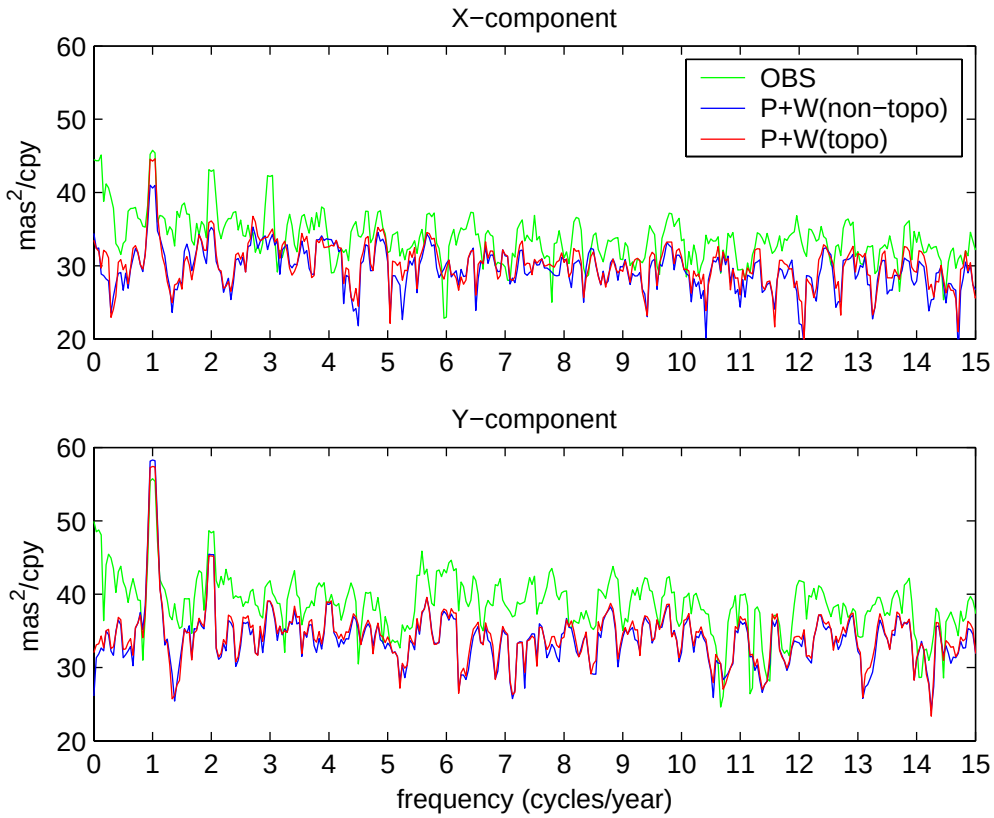
X−component
OBS
P+W(non−topo)
P+W(topo)
mas2/cpy
Y−component
mas2/cpy
frequency (cycles/year)

Figure 12

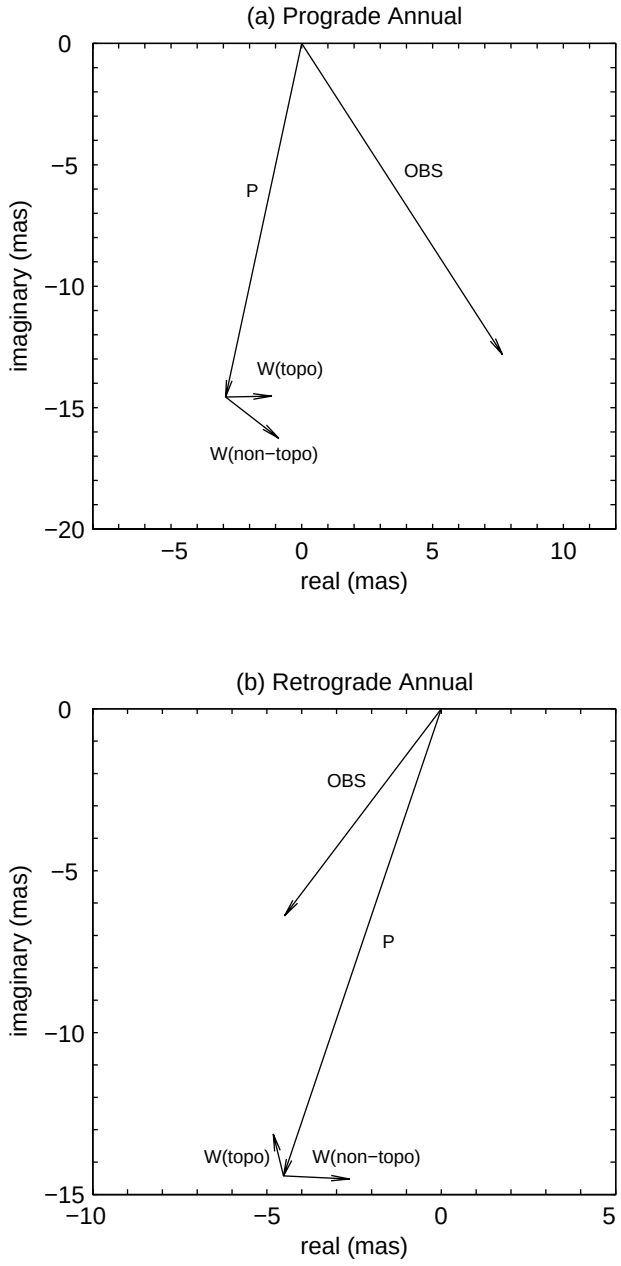
(a) Prograde Annual
0
−5
−10
−15
−20
imaginary (mas)
−5
0
5
10
real (mas)
P
OBS
W(topo)
W(non−topo)
(b) Retrograde Annual
0
−5
−10
−15
imaginary (mas)
−10
−5
0
5
real (mas)
OBS
P
W(topo)
W(non−topo)

Figure 13

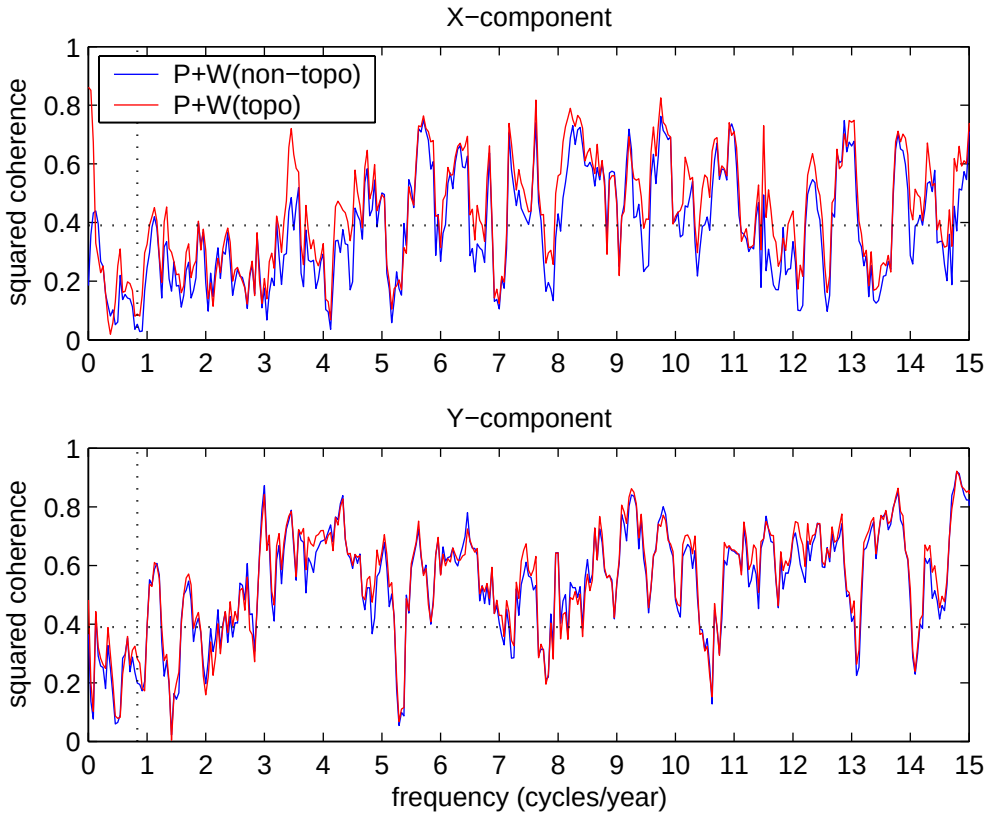
X−component
P+W(non−topo)
P+W(topo)
squared coherence
Y−component
squared coherence
frequency (cycles/year)

Figure 14